8
Estimation of magnetisation direction by magnetic component symmetry analysis

C.A. Foss, K.B. McKenzie and D.A. Clark

ABSTRACT

We present a novel analysis of magnetic field data to provide estimates of magnetisation direction. Starting with measured total magnetic intensity (TMI) data the analysis requires a wavenumber domain transform to produce a dataset of three orthogonal field components. Each of those three field components can in turn be resolved into three terms of different symmetry which in combination characterise specific components of magnetisation. Relative strengths of the magnetisation components (and thereby magnetisation direction) can be derived from strengths of the isolated field component terms. Analysis is ideally performed on bodies of circular or fourfold symmetry about a vertical axis but is tolerant of moderate departures from this shape assumption (a ratio of 2 in maximum to minimum horizontal extent is typically associated with an error of less than 10° in recovered magnetisation direction). Prior removal of an anomaly from its background field by regional-residual separation is recommended if variation in the background field is significant compared to the anomaly amplitude. We present analyses successfully applied to forward computed fields of complex but symmetric bodies of defined magnetisation and to the Black Hill Norite anomaly in South Australia for which we have palaeomagnetic measurements and alternative magnetic field analyses and inversions.

8.1 INTRODUCTION

Subsurface magnetisations causing local variations in the Earth's magnetic field are generally of unknown direction and this complicates their interpretation and mapping of their distribution. Many methods are used to resolve magnetisation direction from analysis of magnetic field data as reviewed by Clark (2014). The theoretical basis that it is possible to recover valid estimates of magnetisation direction directly from magnetic field data is provided by Helbig (1963) who established that the magnetic moment of a body of magnetisation can be determined from the moment integrals of the B_n, B_e, B_d magnetic field components about a point directly above the centre of magnetisation. The approximate centre of a compact magnetisation can be determined by application of transforms to the total gradient or normalised source strength (Beiki *et al.* 2012). Helbig analysis itself can be adapted to provide magnetisation estimates (Schmidt and Clark 1998; Phillips 2005; Phillips *et al.* 2007; Caratori Tontini and Pedersen 2008; Clark 2014) but the method is highly sensitive to separation of the anomaly from the background field. Approximate relationships based on derivatives of the field components (Phillips *et al.* 2007) reduce this influence of the background field. Other methods to estimate magnetisation direction from magnetic field data include those by Fedi *et al.* (1994), Dannemiller and Li (2006) and McKenzie *et al.* (2012). Magnetic

field inversion is a computationally intensive process of estimating magnetisation direction that provides the highest discrimination in resolving magnetisation direction as long as appropriate attention is paid to isolating anomalies of interest from their background fields and expert guidance is applied throughout the inversion process. Both parametric inversion (Foss 2006, 2017; Foss and McKenzie 2011; Pratt *et al*. 2014) and voxel inversion (Paine *et al*. 2001; Lelièvre and Oldenburg 2009; Li 2012; Fullagar and Pears 2015) have been applied to estimation of magnetisation direction from magnetic field data.

Our analysis to determine magnetisation direction shares several key features with Helbig's. Both methods require location of the horizontal centre of magnetisation, both utilise splitting of the field into three orthogonal components, and both recover estimates of the relative strengths of the magnetisation components from integral measures of the strength of magnetic field components. Where the Helbig method uses integral moments of the field components we use the grid standard deviations. Our method also differs from Helbig's in splitting field components into contributions from different magnetisation components according to their symmetry characteristics.

8.2 EQUIVALENCE OF THE GRAVITY GRADIENT TENSOR AND THE MAGNETIC FIELD – MAGNETISATION MATRIX

8.2.1 The gravity gradient tensor for a point mass

The gravity gradient tensor **G**(**r**)at an observation point $\mathbf{r} = (x, y, z)^T$ due to a point mass M positioned at the origin is (see for example Pedersen and Rasmussen 1990; Dransfield 1994):

$$\mathbf{G}(\mathbf{r}) = \gamma M \begin{pmatrix} \frac{3x^2 - r^2}{r^5} & \frac{3xy}{r^5} & \frac{3xz}{r^5} \\ \frac{3xy}{r^5} & \frac{3y^2 - r^2}{r^5} & \frac{3yz}{r^5} \\ \frac{3xz}{r^5} & \frac{3yz}{r^5} & \frac{3z^2 - r^2}{r^5} \end{pmatrix} = \gamma M\, \mathbf{T}(\mathbf{r})$$

(Eqn 8.1)

where γ is the universal gravitational constant and **T**(**r**) is a symmetric matrix of Green's functions. Furthermore, when the x, y, z Cartesian axes are aligned in the north, east and vertically downward directions then **T**(**r**) is

$$\mathbf{T}(\mathbf{r}) = \begin{pmatrix} T_{nn} & T_{ne} & T_{nd} \\ T_{en} & T_{ee} & T_{ed} \\ T_{dn} & T_{de} & T_{dd} \end{pmatrix} = \begin{pmatrix} \frac{3x^2 - r^2}{r^5} & \frac{3xy}{r^5} & \frac{3xz}{r^5} \\ \frac{3xy}{r^5} & \frac{3y^2 - r^2}{r^5} & \frac{3yz}{r^5} \\ \frac{3xz}{r^5} & \frac{3yz}{r^5} & \frac{3z^2 - r^2}{r^5} \end{pmatrix}$$

(Eqn 8.2)

8.2.2 The 3 × 3 magnetic field–magnetisation matrix for a dipole

The expression for the magnetic field vector **B**(**r**) at an observation point $\mathbf{r} = (x, y, z)^T$ due to a point dipole source possessing a magnetic moment **m** located at the origin is given by Blakely (1995, p. 75) as:

$$\mathbf{B}(\mathbf{r}) = \frac{C_m}{r^3}\left\{3\,(\mathbf{m}\cdot\hat{\mathbf{r}})\,\hat{\mathbf{r}} - \mathbf{m}\right\}, \quad \text{(Eqn 8.3)}$$

where $\hat{\mathbf{r}}$ is the unit vector along the line joining the dipole to the observation point, i.e.

$$\hat{\mathbf{r}} = \frac{\mathbf{r}}{|\mathbf{r}|} = \left(\frac{x}{r}, \frac{y}{r}, \frac{z}{r}\right)^T ; r = |\mathbf{r}| = \sqrt{x^2 + y^2 + z^2} \text{ and } r \neq 0.$$

and where C_m is a constant which depends on the system of electromagnetic units used (see Blakely 1995, pp. 67–68). In the International Standard (SI) system of units, C_m = 100 nH/m or 100 nTm/A for magnetic fields expressed in nanotesla (nT), magnetic moments expressed in ampere metre squared (Am^2); and magnetisations expressed in ampere per meter (A/m). The coordinate system adopted here follows the International Geomagnetic Reference Field convention, i.e. *x* is north, y is east and z is vertically down. The Cartesian components of the magnetic field vector are

$$B_x(\mathbf{r}) = \frac{C_m}{r^3}\left\{3\left(\mathbf{m}\cdot\hat{\mathbf{r}}\right)\frac{x}{r} - m_x\right\} = \frac{C_m}{r^3}\left\{3\left(\frac{m_x x^2}{r^2} + \frac{m_y xy}{r^2} + \frac{m_z xz}{r^2}\right) - m_x\right\}. \quad \text{(Eqn 8.4.1)}$$

$$B_y(\mathbf{r}) = \frac{C_m}{r^3}\left\{3\left(\mathbf{m}\cdot\hat{\mathbf{r}}\right)\frac{y}{r} - m_y\right\} = \frac{C_m}{r^3}\left\{3\left(\frac{m_x xy}{r^2} + \frac{m_y y^2}{r^2} + \frac{m_z yz}{r^2}\right) - m_y\right\}. \quad \text{(Eqn 8.4.2)}$$

$$B_z(\mathbf{r}) = \frac{C_m}{r^3}\left\{3\left(\mathbf{m}\cdot\hat{\mathbf{r}}\right)\frac{z}{r} - m_z\right\} = \frac{C_m}{r^3}\left\{3\left(\frac{m_x xz}{r^2} + \frac{m_y yz}{r^2} + \frac{m_z z^2}{r^2}\right) - m_z\right\}. \quad \text{(Eqn 8.4.3)}$$

For a series of magnetic dipole moments **m** directed along the north, east and downward vertical directions, i.e. $\mathbf{m}_x = m\hat{\mathbf{x}}$; $\mathbf{m}_y = m\hat{\mathbf{y}}$; $\mathbf{m}_z = m\hat{\mathbf{z}}$, or alternatively for a series of magnetisations $\mathbf{J}_n = J\hat{\mathbf{x}}$, $\mathbf{J}_e = J\hat{\mathbf{y}}$, $\mathbf{J}_d = J\hat{\mathbf{z}}$ for a uniformly magnetised sphere of volume v and magnetisation intensity $J = m/v$, the expressions for the north, east and downward vertical components of the magnetic field due to each of the three orthogonal magnetisations may be formulated as a matrix equation as follows:

$$\mathbf{B_m} = \begin{pmatrix} B_n^{Jn} & B_e^{Jn} & B_d^{Jn} \\ B_n^{Je} & B_e^{Je} & B_d^{Je} \\ B_n^{Jd} & B_e^{Jd} & B_d^{Jd} \end{pmatrix}$$

$$= \mathrm{C_m} m \begin{pmatrix} \frac{3x^2 - r^2}{r^5} & \frac{3xy}{r^5} & \frac{3xz}{r^5} \\ \frac{3xy}{r^5} & \frac{3y^2 - r^2}{r^5} & \frac{3yz}{r^5} \\ \frac{3xz}{r^5} & \frac{3yz}{r^5} & \frac{3z^2 - r^2}{r^5} \end{pmatrix} = \mathrm{C_m} m \mathbf{T}(\mathbf{r}),$$

(Eqn 8.5)

where **T**(**r**) is the (3 × 3) symmetric matrix of Green's functions specified in Eqn 8.2. The matrix $\mathbf{B_m}$ is known as the magnetic field-magnetisation matrix. Its three rows are the magnetic field components B_n, B_e and B_d for each of the $\mathbf{J_n}$, $\mathbf{J_e}$ and $\mathbf{J}_d$ magnetisations. Importantly, since **T**(**r**) is related to the gravity gradient tensor of a point mass (or uniform sphere with density ρ and mass $M = \rho v$) by the relation $\mathbf{G}(\mathbf{r}) = \gamma M \mathbf{T}(\mathbf{r})$, then the magnetic field-magnetisation matrix $\mathbf{B_m}$ may be expressed in terms of the gravity gradient tensor **G**(**r**) namely,

$$\mathbf{B_m} = \begin{pmatrix} B_n^{Jn} & B_e^{Jn} & B_d^{Jn} \\ B_n^{Je} & B_e^{Je} & B_d^{Je} \\ B_n^{Jd} & B_e^{Jd} & B_d^{Jd} \end{pmatrix} = \mathrm{C_m} m \mathbf{T}(\mathbf{r})$$

$$= \left(\frac{\mathrm{C_m} m}{\gamma M}\right)\mathbf{G}(\mathbf{r}) = \left(\frac{\mathrm{C_m} J}{\gamma \rho}\right)\mathbf{G}(\mathbf{r}). \quad \text{(Eqn 8.6)}$$

The spatial patterns of the gradient tensor elements in Eqn 8.1 and the magnetic components in Eqn 8.5 are identical, as is the symmetry and anti-symmetry of their individual terms about the north and east axes (as is evident from considering the consequence of change of sign in the x and y coordinates respectively). The map representations of these functions are shown in Fig 8.1A and 8.1B.

8.2.3 An expression for magnetisation direction

The direction of magnetisation (or magnetic moment) for a uniformly magnetised body with magnetisation **J** is defined by a declination D_J or azimuthal angle measured positive clockwise from true north to the horizontal projection of the magnetisation vector **J** and an inclination angle I_J which is the angle between the magnetisation vector **J** and its horizontal projection measured positive downwards. An expression for the declination of magnetisation (or of magnetic moment) at any point **r** = (0, 0,−z)^T above the point dipole or centre of a magnetised sphere is obtained from the ratio of the horizontal magnetic field components as shown in Chapter 7.

$$D_J = \arctan\left(\frac{J_e}{J_n}\right) = \arctan\left(\frac{-B_e}{-B_n}\right) \quad \text{for } 0 \le D_J \le 2\pi.$$

(Eqn 8.7)

An expression for the inclination of magnetisation I_J is obtained from the ratio of the horizontal field component $B_h = \sqrt{B_n^2 + B_e^2}$ to half the vertical field component B_d as shown in Foss *et al*. (2021)

$$I_J = \arctan\left(\frac{J_d}{J_h}\right) = \arctan\left(\frac{B_d}{2\sqrt{B_n^2 + B_e^2}}\right) \quad \text{for } -\frac{\pi}{2} \le I_J \le \frac{\pi}{2}.$$

(Eqn 8.8)

8.2.4 Poisson's relationship between gravity and magnetic fields

Poisson's relation states that if the boundaries of a gravitational and magnetic source are identical and if the density and magnetisation are uniform within those sources, then the magnetic scalar potential is proportional to the component of gravitational attraction in the direction of magnetisation (Blakely 1995). An expression for the magnetic scalar potential V(**r**) of a uniform body with volume v, density ρ and magnetisation **J** may be derived from the Poisson's relation as follows (Blakely 1995, pp. 91–93):

$$\mathrm{V}(\mathbf{r}) = -\mathrm{C_m}\left(\frac{1}{\gamma M}\right)\nabla \mathrm{U}(\mathbf{r}) \cdot \mathbf{m} = -\left(\frac{\mathrm{C_m}}{\gamma \rho}\right)\mathbf{g}^T(\mathbf{r}) \cdot \mathbf{J}, \quad \text{(Eqn 8.9)}$$

where $\mathbf{g}^T(\mathbf{r})$ denotes the transpose of the gravity field vector. For a magnetic dipole with moment **m** or a magnetic sphere with uniform magnetisation **J**, density ρ and equivalent mass M, its magnetic scalar potential V(**r**) is

$$\mathrm{V}(\mathbf{r}) = \frac{\mathrm{C_m}}{r^3}(m_x x + m_y y + m_z z) \quad \text{(Eqn 8.10)}$$

Expressions for the anomalous magnetic field vector are derived by taking the gradient of the magnetic scalar potential in Eqn 8.9, then

$$\mathbf{B}(\mathbf{r}) = -\nabla V(\mathbf{r}_p) = \left(\frac{C_m}{\gamma\rho}\right)\nabla \mathbf{g}^T(\mathbf{r})\cdot\mathbf{J}$$
$$= \left(\frac{C_m}{\gamma\rho}\right)\mathbf{G}^T(\mathbf{r})\cdot\mathbf{J} = C_m\,\mathbf{T}^T(\mathbf{r})\cdot\mathbf{J}, \quad \text{(Eqn 8.11)}$$

where $\mathbf{T}^T(\mathbf{r}_p)$ is the transpose of matrix $\mathbf{T}(\mathbf{r}_p)$ at an external measurement point.

For a northerly magnetisation $\mathbf{J} = J\,\hat{\mathbf{x}}$ and from the expressions for $\mathbf{T}(\mathbf{r}_p)$ in Eqn 8.5, the components of the magnetic field vector obtained from Eqn 8.11 agree with the expressions for $B_n^{In}, B_e^{In}, B_d^{In}$ in the first row of matrix Eqn 8.6. Similar agreements with $B_n^{Je}, B_e^{Je}, B_d^{Je}$ in the second row of matrix Eqn 8.6 are obtained from Eqn 8.11 for an easterly magnetisation $\mathbf{J} = J\,\hat{\mathbf{y}}$ and also with $B_n^{Jd}, B_e^{Jd}, B_d^{Jd}$ in the third row of matrix Eqn 8.6 for a downward vertical magnetisation $\mathbf{J} = J\,\hat{\mathbf{z}}$. These results are in agreement Pedersen and Bastani (2016). In conclusion the results shown in Sections 2.1 and 2.2 are consistent with and proven by an application of Poisson's relation.

8.3 MAGNETIC COMPONENT SYMMETRY (MCS) ANALYSIS

Grids of total magnetic intensity (TMI) can be resolved into grids of three orthogonal components J_e (east), J_n (north) and J_d (down) (Lourenço and Morrison 1973). We have established that for a dipole the 3 × 3 matrix of magnetic field components due to orthogonal magnetisation components of equal strength (magnetisation direction of

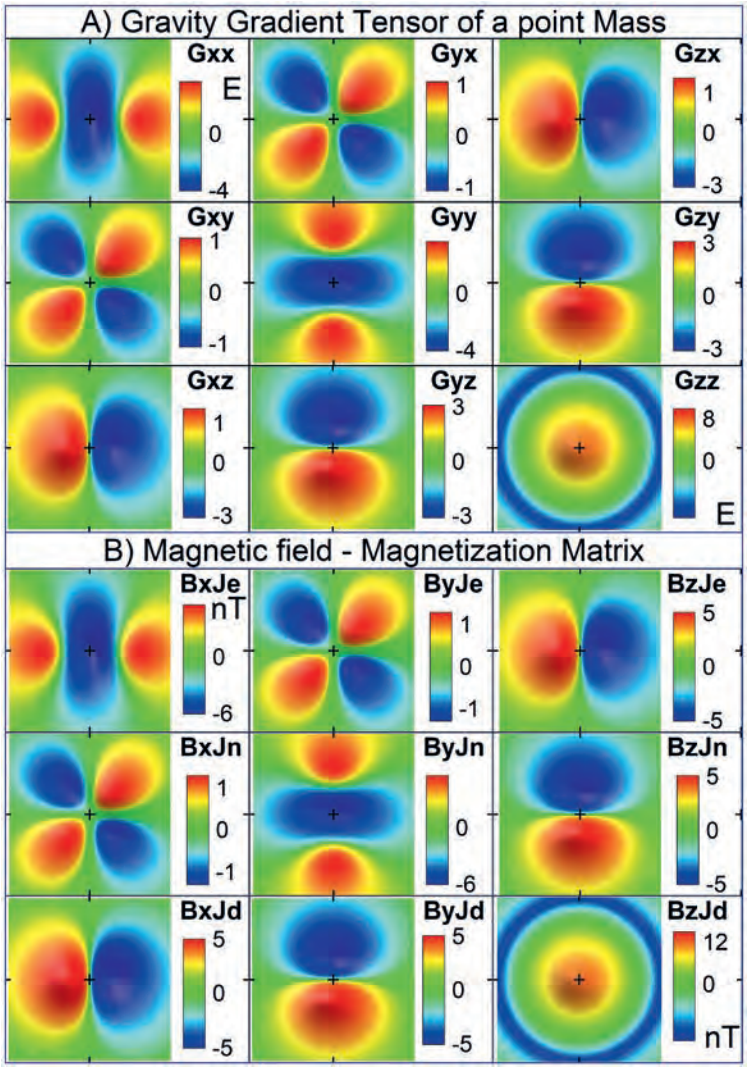

Fig. 8.1. A) Gravity gradient tensor of a point mass, and B) matrix of magnetic field components M_iJ_k where i = x,y,z and k = e,n,d are indices of the field and magnetisation respectively.

declination 45°, inclination +35.3°) is equivalent to the gravity gradient tensor of a point mass, with one-to-one equivalence between individual elements. The individual terms of the gravity gradient tensor and the magnetic field–magnetisation matrix are characterised by their symmetry patterns in the horizontal plane, with individual elements belonging to one of three symmetry classes: symmetric and antisymmetric about two orthogonal planes, antisymmetric about two orthogonal planes, or symmetric about two orthogonal planes (including full circular symmetry) as expressed in the individual terms of Eqns (8.1) and (8.5). The vertical magnetic field component B_d comprises two contributions with single axis anti-symmetry (B_d^{Jn} and B_d^{Je}) and a third contribution (B_d^{Jd}) with full circular symmetry. The two horizontal components: B_n and B_e are comprised of one contribution of single axis anti-symmetry (B_n^{Jd} and B_e^{Jd} respectively), one contribution of two axes symmetry (B_n^{Jn} and B_e^{Je} respectively), and one contribution of two axes anti-symmetry (B_n^{Je} and B_e^{Jn} respectively). In all three cases the magnetic field components can be uniquely deconstructed into these three contributions of different symmetry and the polarities and relative strengths of those separate field contributions reveal the polarities and relative strengths of the causative magnetisation components.

Figure 8.2 shows a selection of magnetisations suitable for MCS analysis, each with its central vertical axis: A) a dipole (magnetisation component field contributions shown in Fig. 8.1B), B) ellipsoids with two equal horizontal axes, C) circular-section vertical cylinders, D) a square ring (TMI anomaly shown in Fig. 8.4B), E) a NE-SW and SE-NW cross (TMI anomaly shown in Fig. 8.4A), and F) multiple horizontal symmetry bodies on a common vertical axis (TMI anomaly shown in Fig. 8.7A). The ellipsoids and cylinders have horizontal diameter to depth extent ratios of 1:5 and 5:1 to detect any sensitivity to depth extent not tested in the dipole analysis.

MCS analysis is performed by transforming a measured TMI anomaly into its orthogonal field components and then resolving those field components into contributions from magnetisation components assigned according to their symmetry patterns. The analysis is performed by estimating the centre of magnetisation (usually by applying an NSS or total gradient transform to highlight the anomaly centre), flipping the grids about east–west and north–south axes through this point, and variously summing or differencing the original and flipped grids. Comparison of the standard deviations of grids with different symmetry pattern requires correction that is dependent on the horizontal extent of the grids. A convenient methodology to avoid this problem is to operate on pairs of component grids with identical symmetry pattern. The sequence of operations is presented in Table 8.1 leading to estimation of declination and inclination of magnetisation from ratios of the standard deviations of the grids (steps 15 and 16). Summing flipped grids tends to cancel regional field differences of that orientation extending across the area of analysis, but differencing the flipped grids retains any parallel regional field variation in the original ratio to the differenced anomaly component. A regional-residual separation should be performed before the MCS analysis for any grids superimposed on a regional field gradient significant in relation to the anomaly amplitude.

Comparison of magnetic field components across a horizontal plane best suits investigation of the horizontal components of magnetisation and the declination of magnetisation. We derive three declination estimates from grid standard deviation ratios of: (i) horizontal field components due to co-parallel magnetisations B_e^{Je} and B_n^{Jn}, (ii) horizontal field components due to cross-horizontal magnetisations B_e^{Jn} and B_n^{Je}, and (iii) vertical field components due to horizontal magnetisations B_d^{Je} and B_d^{Jn}. Note that these three estimates are by no means independent but each is influenced differently by imperfection in the analysis and the mean of the three estimates is more robust than their individual values. The declination of magnetisation is derived from the arctangent of the ratio of the various grid standard deviations as listed in step 15 of Table 8.1.

Estimation of the inclination of magnetisation is more complex and requires multiple grid operations. The vertical component of magnetisation related to inclination angle has a different pattern of influence on the magnetic field measured across a horizontal surface than do the

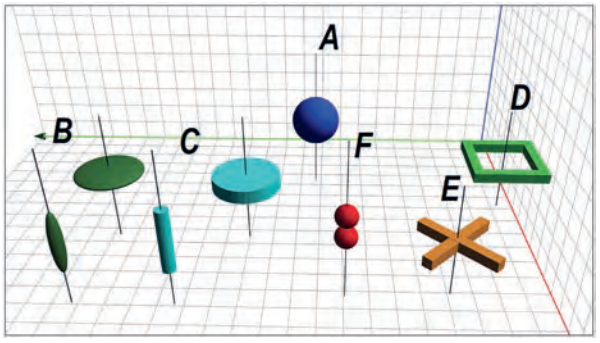

Fig. 8.2. Selection of magnetisation bodies suitable for MCS analysis.

Table 8.1. Sequential processing steps of MCS analysis.

Step	Operation
Initial processing	
1	Regional-residual anomaly separation (recommended)
2	FFT phase transform TMI to B_n, B_e, B_d
3	Centre the anomaly and clip B_n, B_e, B_d to square grids
Grid flip + compute	
4	Flip B_d E-W, B_d^{Je} = (B_d – B_d E-W flip)/2, fd = (B_d + B_d E-W flip)/2
5	Flip fd N-S, B_d^{Jd} = (fd + fd N-S flip)/2
6	Flip Bd N-S, B_d^{Jn} = (B_d – B_d N-S flip)/2
7	Flip B_e E-W, B_e^{Je} = (B_e + B_e E-W flip)/2, fe = (B_e – B_e E-W flip)/2
8	Flip B_n N-S, B_n^{Jn} = (B_n + B_n N-S flip)/2, fn = (B_n – B_n N-S flip)/2
9	Flip fe N-S, Flip fn E-W (generating grids flipped in 2 directions)
10	B_e^{Jd} = (fe + fe N-S flip)/2, B_e^{Jn} = (fe - fe N-S flip)/2
11	B_n^{Jd} = (fn + fn E-W flip)/2, B_n^{Je} = (fn - fn E-W flip)/2
Calculate from grid standard deviations	
12	B_h^{Jd} = sqrt(B_e^{Jd} ^2 + B_n^{Jd} ^2), B_d^{Jh} = sqrt(B_d^{Je} ^2 + B_d^{Jn} ^2)
13	B_e^{Jh} = sqrt(B_e^{Je} ^2 + B_e^{Jn} ^2), B_n^{Jh} = sqrt(B_n^{Je} ^2 + B_n^{Jn} ^2)
14	B_h^{Jh} = sqrt(B_e^{Jh} ^2 + B_n^{Jh} ^2)
15	Declination 1 = arctangent (B_e^{Jn}, B_n^{Je}) Declination 2 = arctangent (B_n^{Jn}, B_e^{Je}) Declination 3 = arctangent (B_d^{Jn}, B_d^{Je})
16	Inclination 1 = arctangent (B_d^{Jd}, B_d^{Jh} *sqrt(2)) Inclination 2 = arctangent (B_h^{Jd}, B_d^{Jh} *sqrt(2)) Inclination 3 = arctangent (B_h^{Jd}, B_h^{Jh} *sqrt(2))

horizontal components and therefore recovery of the inclination angle faces different challenges. To investigate fidelity in recovering estimates of inclination of magnetisation we generated magnetic fields from a dipole located at a depth of 100 m with the field computed over a grid of side length 1 km for magnetisations with a range of declinations and inclinations in a −60° geomagnetic inclination field. MCS analysis was applied to component grids derived by FFT of the computed TMI. The resulting inclination estimates are independent of declination, which for this noise-free data was recovered closely even at inclinations up to 80°. The ratio of vertical to horizontal components of magnetisation from which we derive inclination angle climbs steeply at high inclinations (Fig. 8.3A) but the error in the resulting inclination estimate is maximum at mid inclinations (Fig. 8.3B). Errors in individual inclination estimates were in all cases less than 2° and errors in the mean of the three estimates were in all cases less than 1°. We also applied the analysis to fields forward computed from the ellipsoids and circular cylinders shown in Figs 8.2B and 8.2C with depth extent to diameter ratios of 5:1 and 1:5 and reliably recovered both declination and inclination estimates for magnetisations of shallow, mid and steep inclinations of 15°, 45° and 75° respectively with similar precision to recovery of magnetisation direction for the dipole models. The relationships to derive inclination of magnetisation from ratios of grid standard deviation values are listed in step 16 of Table 8.1.

Extension to more complex but still symmetric magnetisations is illustrated for the rectangular ring and diagonal cross magnetisation distributions shown in Fig. 8.2D and 8.2E. Note that for bodies of symmetry about two orthogonal planes but where those planes are not coincident with the east–west and north–south coordinate axes, that ideal symmetry can be achieved by a suitable rotation of the coordinate system to be coincident with the grid reflection axes and a subsequent reverse rotation of the recovered declination angle (but we show later that this adjustment is not necessary). Forward computed TMI anomalies for the diagonal cross and square ring magnetisations in a geomagnetic field of inclination −60° are shown in Fig. 8.4. The cross body is given a magnetisation of declination 60°, inclination +30°. For this low-inclination magnetisation in a moderately steep geomagnetic field the anomaly pattern is

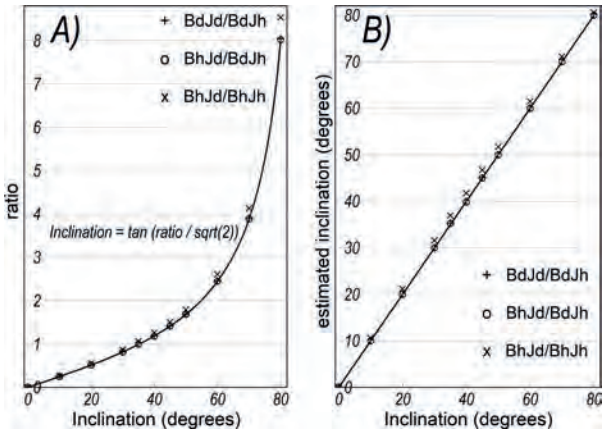

Fig. 8.3. A) ratio of magnetic field component grid standard deviations and B) corresponding inclination angles against angle of inclination of magnetisation.

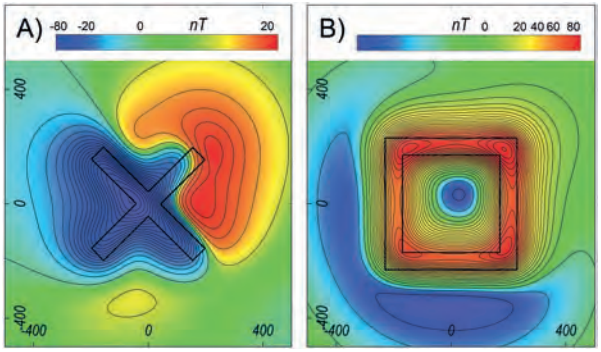

Fig. 8.4. TMI images in a 60° south geomagnetic field over A) a diagonal cross body of magnetisation 60°, +30° and B) a square ring body of magnetisation 120°, −70°.

determined primarily by the declination of magnetisation. The square ring body is given a magnetisation of declination 120°, inclination −70°. For this steep inclination the anomaly pattern is dominated by the spatial distribution of the magnetisation. The two bodies have horizontal widths of 400 to 450 m, depth to the top of the magnetisation of 100 m, and depth extent of 60 m. The grids have a side length of 1 km. The computed TMI anomalies were transformed to B_n, B_e and B_d grids which were then used in MCS analysis following the operations listed in Table 8.1. For both bodies each individual estimate of declination was recovered to within one degree. Individual inclination estimates were recovered to within two degrees, with the mean of the three estimates within one degree. The magnetic component–magnetisation matrix for the diagonal cross body is shown in Fig. 8.5. The body outline is added to the grid images for reference but is not used in the analysis. Figure 8.6 shows the MCS analysis form we use to collate results. The top left section is a map of grid polarities expected for +ve magnetisation components. In this case there is a complete match with polarity of the recovered grids showing that the magnetisation has +ve inclination and is in the first quadrant (declination 0 to 90°). The grids are quantified by their standard deviation values (annotated in blue in Fig. 8.6) which provide more reliable measures than the peak-to-trough ranges which for measured data are more susceptible to local distortion. The three declination estimates (annotated in red in Fig. 8.6) are derived from ratios of grid standard deviation values together with the grid polarities. Estimation of inclination requires further processing as specified in steps 12 to 14 of Table 8.1. We take the mean declination and inclination values as the best estimated magnetisation direction.

Because magnetic fields are additive MCS analysis can be extended to constructions of symmetric magnetisations centred on a common vertical axis (as for Fig. 8.2 example F). In the case of bodies with identical magnetisation direction the analysis returns that direction as it does for an individual body. The case of bodies with different magnetisation direction is more complex. Figure 8.7A shows a TMI anomaly computed over two dipoles with a difference in magnetisation direction of 150°. The deeper dipole is at a depth of 4,000 m. The shallower dipole directly above it at a depth of 3,200 m has a 50% smaller magnetic moment. By visual inspection the TMI image is more complex than expected for a single dipole but there is no obvious indication that it is due to two magnetisations of such different direction. Figure 8.7B shows the B_d^{Jn} grid from MCS analysis. This image clearly reveals the contrasting J_n component polarities of the two differently directed magnetisations with the centre of the image expressing the shallower magnetisation and the outer section of the image expressing the deeper magnetisation. Full MCS analysis reveals the polarity of all three components of both magnetisations. The magnetisation direction recovered from MCS analysis is close to the vector sum of the two magnetisations in a ratio of shallower to deeper of 0.85:1 (compared to 0.5:1 for their magnetisation moments). This ratio represents a preferential 1.7 weighting for the field of the shallower magnetisation. On the central axis there is an inverse cubed weighting of 1.95 for the field of the shallower source and this value decreases continuously with horizontal distance from the axis. For the fields measured 1,000 and 2,000 m shallower over the same magnetisation model MCS analysis

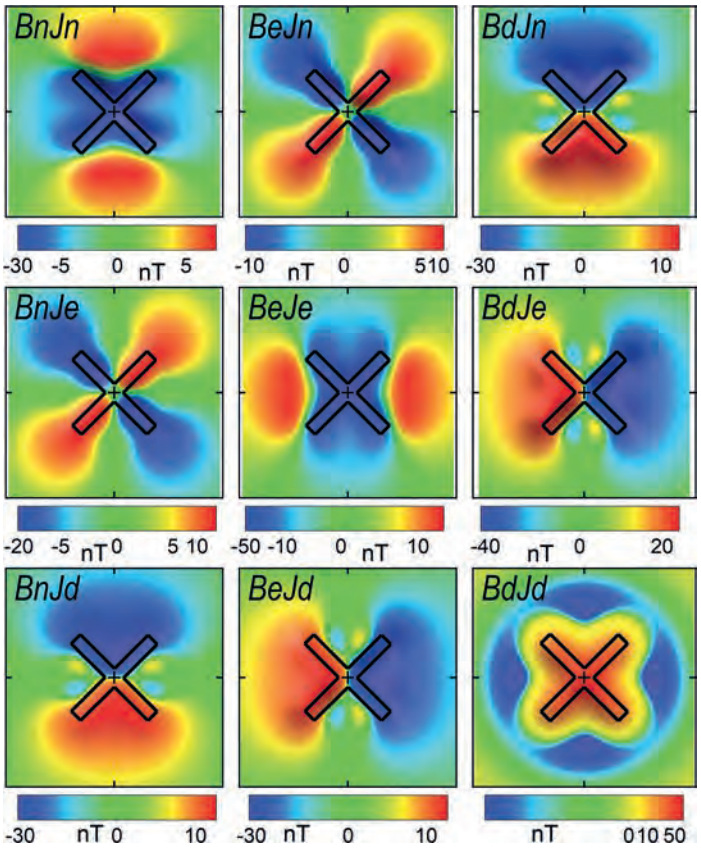

Fig. 8.5. Magnetic field–magnetisation matrix from MCS analysis of the diagonal cross anomaly in Fig. 8.4A.

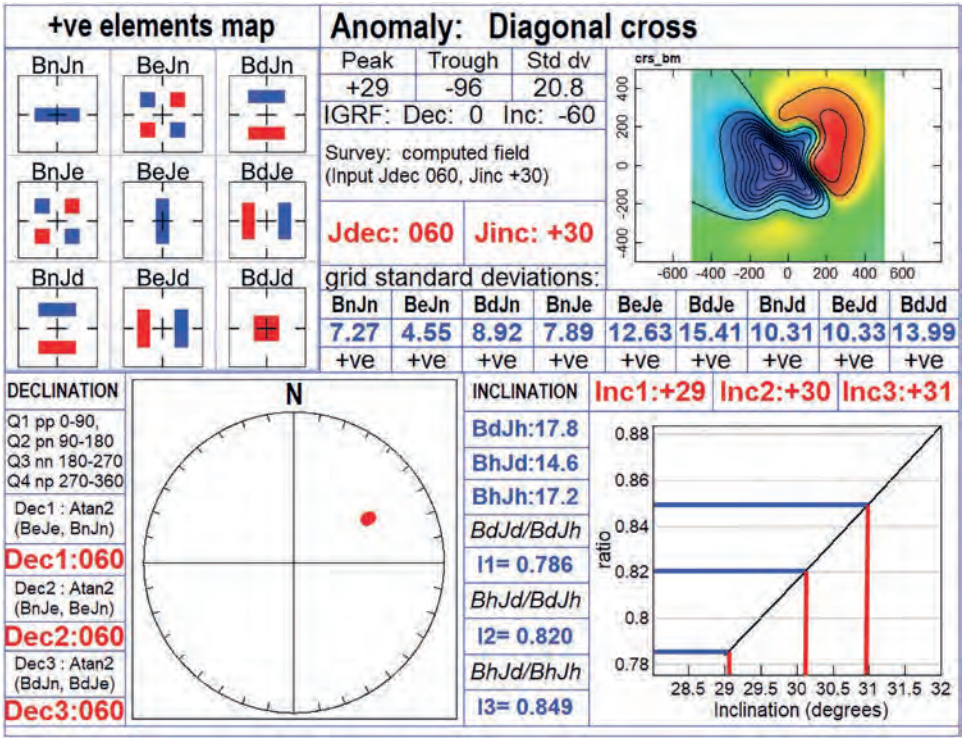

Fig. 8.6. MCS analysis form for the diagonal cross anomaly of Fig. 8.4A.

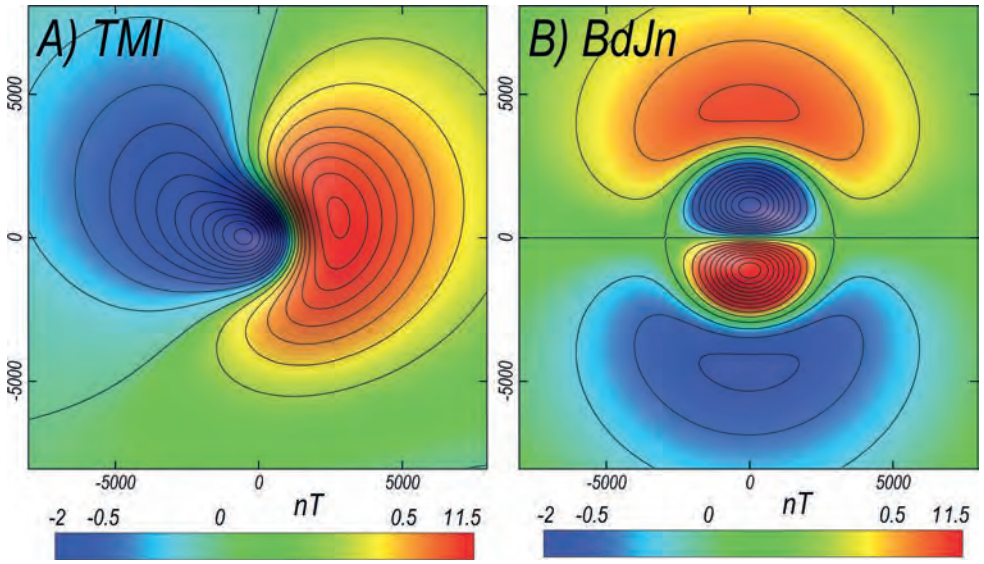

Fig. 8.7. A) TMI image over two vertically stacked magnetisations (see text for details) and B) BdJn image from MCS analysis.

magnetisation direction estimates change by 17° and 43° respectively, moving towards the direction of the shallower magnetisation as the weighting of that magnetisation increases substantially in the lower elevation fields. In these cases MCS analysis does not recover the individual magnetisation directions. However, from fields computed at all three elevations above the model the analysis detects the double magnetisation direction and both the deeper and shallower directions can be assigned declination quadrants and inclination polarities to provide a good starting model for any subsequent inversion studies.

8.4 A CASE STUDY OF THE BLACK HILL NORITE NORTH-WEST ANOMALY, SOUTH AUSTRALIA

The Black Hill Norite also known as the Black Hill Gabbroic Complex is an undeformed, post-tectonic Ordovician intrusion into Cambrian Kanmantoo Group metasediments (Turner 1991). The main lithologies include gabbro, anorthosite, norite, troctolite, peridotite, and diorite. At least some of these rocks have retained a substantial remnant magnetisation that gives rise to distinctive magnetic field anomalies with an equally prominent peak to the south-west and trough to the north-east. Figure 8.8A shows the isolated north-western TMI anomaly of this pattern which we term the BHN-NW anomaly.

Figure 8.8B shows the outline of the parametric inversion model of Foss and McKenzie (2011) over an

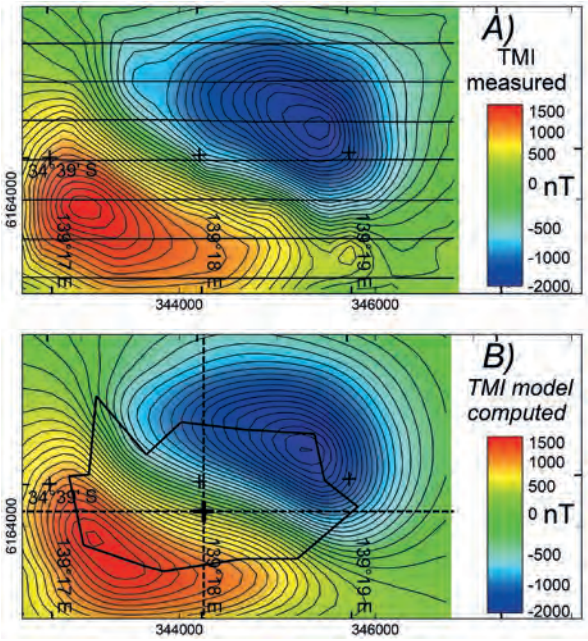

Fig. 8.8. BHN-NW anomaly: A) measured TMI with 400 m spaced E–W flightlines and B) model computed anomaly with the model centre and E–W and N–S grid flip axes shown.

image of TMI computed from the model. The model is a horizontal polygonal sheet of homogeneous magnetisation and its centre was used to locate the N-S and E-W grid flip axes for the MCS analysis. MCS analysis of the BHN-NW anomaly utilises an FFT phase transform of TMI to provide the B_n, B_e and B_d components. As shown in Fig. 8.9 these FFT-derived components are consistent with components forward computed from the TMI inversion model.

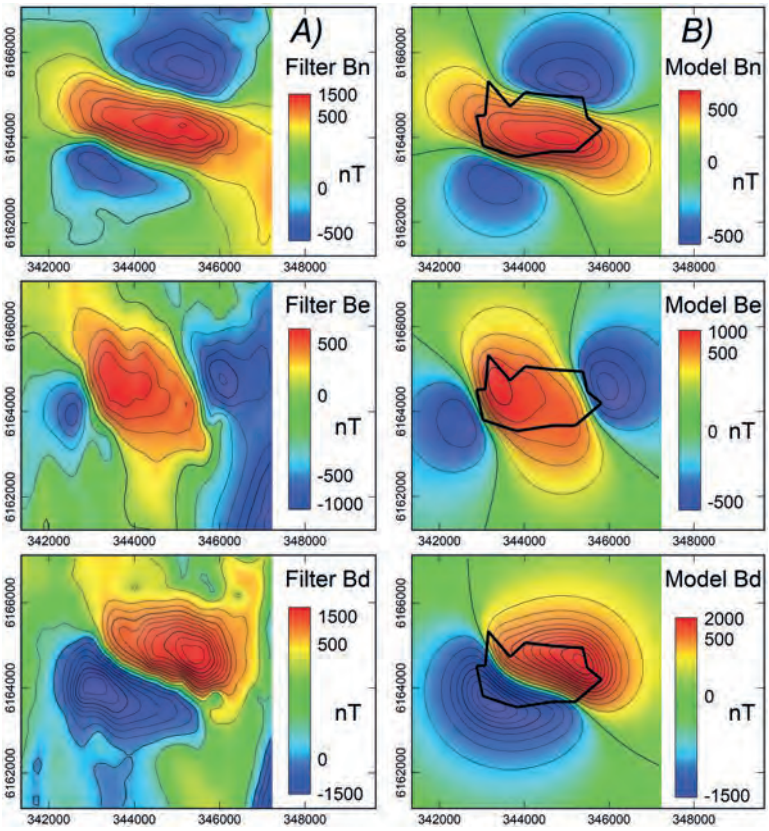

Fig. 8.9. Magnetic field component maps Bn (north), Be (east) and Bd (down): A) derived by FFT analysis of the measured TMI grid and B) forward computed from the inversion model.

MCS analysis was performed on the FFT-derived component grids following the steps listed in Table 8.1. Four steps of the analysis shown graphically in Fig. 8.10 reveal how grids variously symmetric and anti-symmetric are generated by differencing and summing a grid with its reflection. The resulting grids for the nine magnetisation component separations are plotted in Fig. 8.11 using a common linear colour stretch to highlight relative strengths of the grids. The three grids due to the easting magnetisation component (B_n^{Je}, B_n^{Je} and B_d^{Je} in the middle row of Fig. 8.11) and the three grids due to the northing magnetisation component (B_n^{Jn}, B_n^{Jn} and B_d^{Jn} in the top row of Fig. 8.11) have opposite polarity to those for an 'n-e-d' positive magnetisation, and the three grids due to the vertical magnetisation component (B_n^{Jd}, B_n^{Jd} and B_d^{Jd} in the bottom row of Fig. 8.11) have low amplitude consistent with a low positive-inclination magnetisation. The grid standard deviation values are plotted in blue on the MCS analysis form in the lower part of Fig. 8.12 and the resulting declination and inclination estimates are plotted in red. The three declination estimates range between 221° and 237° with a mean of 228°, and the three inclination estimates range between +11° and +13° with a mean of +12°. The MCS analysis best estimate direction is 228°, +12°.

Figure 8.13 is a stereonet plot of estimates of resultant and remnant magnetisation direction obtained by various authors and methods (note that the resultant and remnant directions cannot be directly compared without consideration of the role of induced magnetisation). Palaeomagnetic studies (Rajagopalan *et al.* 1993; Schmidt *et al.* 1993; Schmidt and Clark 1997) used samples recovered from fresh outcrop in a quarry east of the anomaly within an area of similar but more complex magnetic field variation The first resultant magnetisation estimate derived from the BHN-NW anomaly itself by Schmidt and Clark (1997) using Helbig analysis is in good agreement with earlier remanent and induced magnetisation measurements. There has been a subsequent Helbig study of the anomaly (Phillips 2005), a Helbig and parametric inversion study (Foss and McKenzie 2011) and an inversion study (Pratt *et al.* 2014). The resultant magnetisation estimates derived from the anomaly (points B, C, D, E, G in Fig. 8.13) are well grouped about a mean of 226°, +7° which is within 5° of

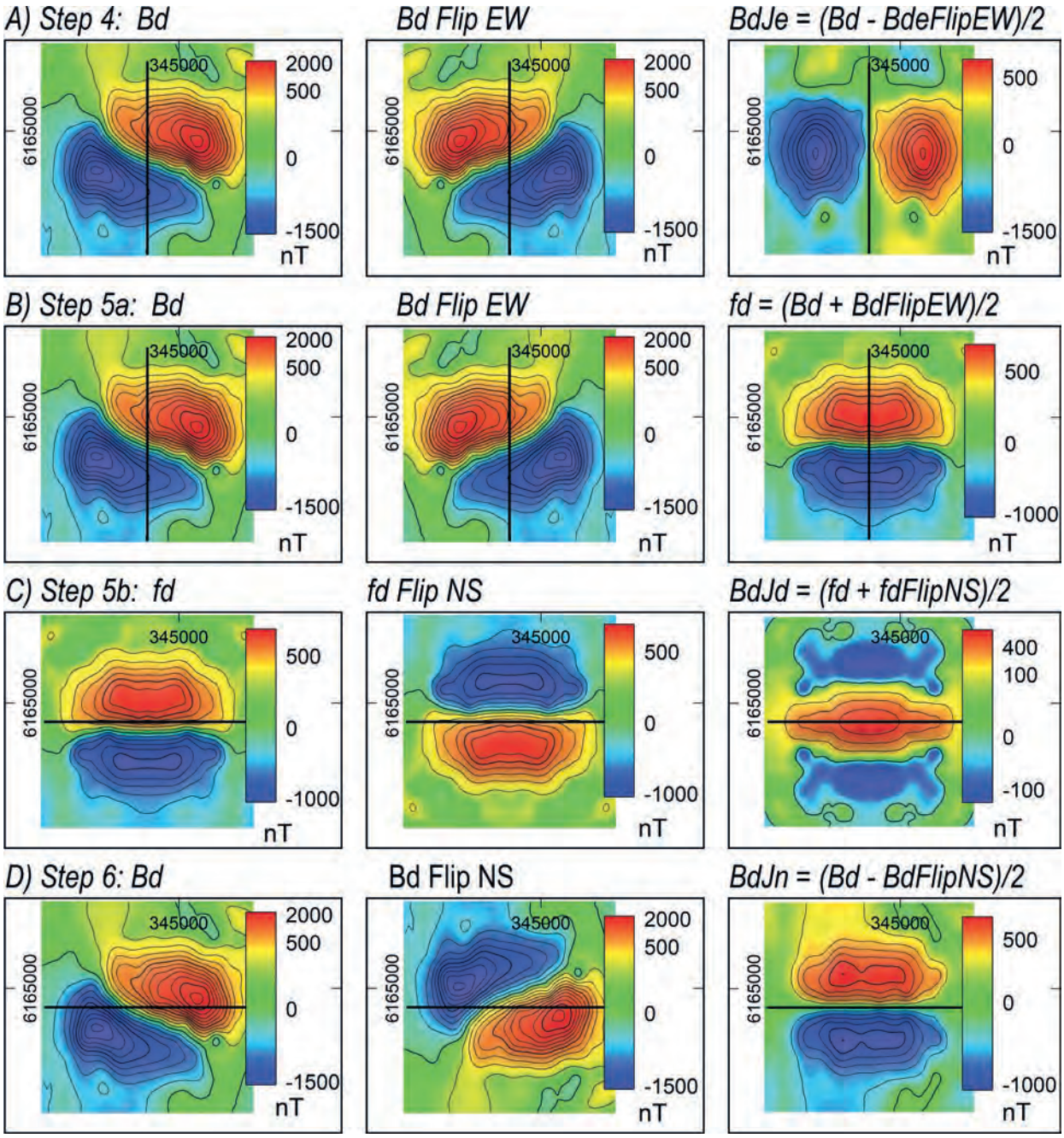

Fig. 8.10. MCS analysis steps 4 to 7 (see Table 8.1) applied to the BHN-NW measured TMI anomaly.

the mean of the three reported remnant magnetisation directions (points I, J, K in Fig. 8.13) of 225°, +12°. This suggests that the magnetisation of the source of the BHN-NW anomaly has a Koenigsberger ratio substantially higher than the value of 2.1 directly measured on samples from the nearby quarry. The MCS analysis direction falls within the population of resultant magnetisation directions from other studies and only 5° from the mean of the other estimates.

The true magnetisation direction of the source of the BHN-NW anomaly is unknown. To evaluate the performance of the MCS method we applied the analysis to the field forward computed from the known magnetisation inversion model of Foss and McKenzie, 2011. The result is presented in Fig. 8.14. The inversion model (body a in Fig. 8.14A) has an average east–west length of 2700 m, average north–south length of 1,500 m and depth to the top of magnetisation below the

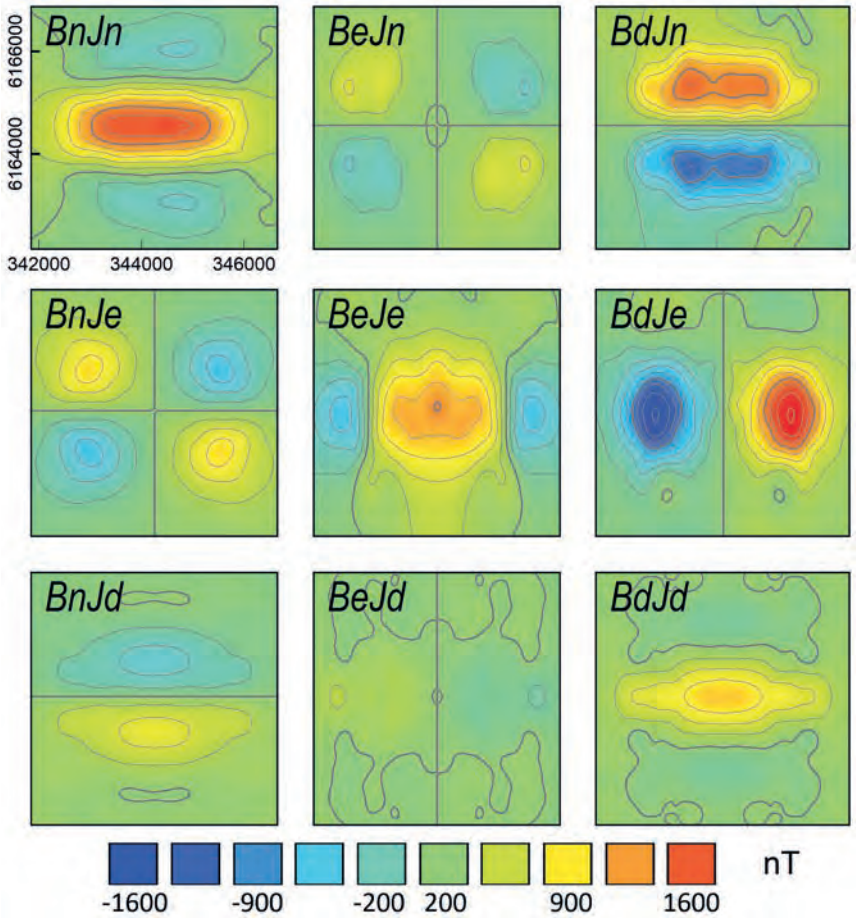

Fig. 8.11. MCS analysis steps 8 to 11 (see Table 8.1) applied to the BHN-NW measured TMI anomaly.

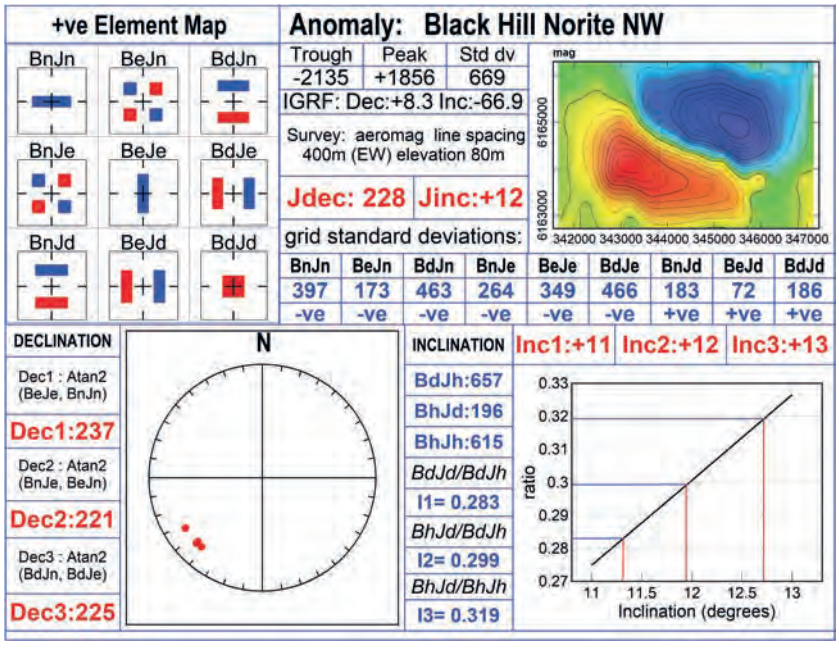

Fig. 8.12. Top) Magnetic field – magnetisation component matrix from MCS analysis of the BHN-NW measured TMI anomaly (all images with a common linear stretch) and Bottom) MCS analysis form with annotated results.

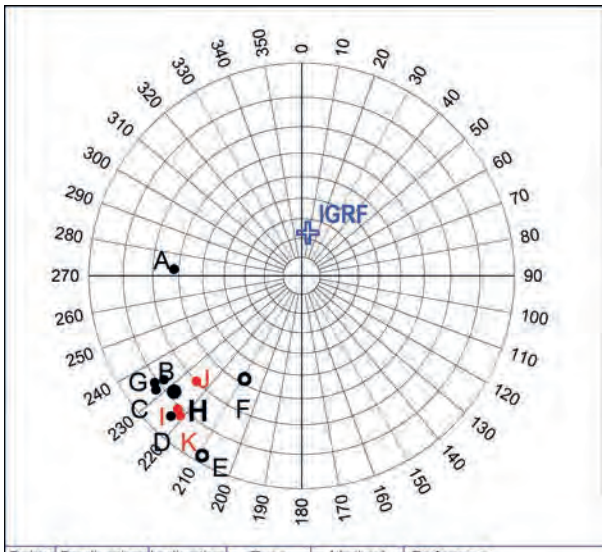

Point	Declination	Inclination	Type	Method	Reference
A	273	+28	resultant	Helbig	Phillips, 2005
B	233	+12	resultant	Helbig	Foss and McKenzie,2011
C	232	+8	resultant	Inversion	Foss and McKenzie,2011
D	223	+6	resultant	Helbig	Foss and McKenzie,2011
E	209	-2	resultant	Helbig	Schmidt and Clark,1997
F	209	-32	resultant	palaeomag	Schmidt and Clark,1997
G	234	+9	resultant	Inversion	Prattt et al, 2014
H	**228**	**12**	**resultant**	**OMC**	**This study**
I	223	+9	remanent	palaeomag	Schmidt et al, 1993
J	231	+20	remanent	palaeomag	Schmidt et al, 1993
K	221	+8	remanent	palaeomag	Rajagopalan et al,1993

Fig. 8.13. Measured remnant (red) and estimated resultant (black) magnetisation directions. Solid symbols are +ve (northern hemisphere) inclination and open symbols are –ve (southern hemisphere) inclination.

measurement plane of 543 m. The error in recovering the input magnetisation direction of the model from MCS analysis of the computed field is 6°. We generated a rectangular prism of the same dimensions and depth (body b in Fig. 8.14A) and also rotated that body by 90° (body c in Fig. 8.14A). For both bodies the magnetisation direction was recovered with an error of only 7°. We also rotated the body clockwise and anticlockwise by 45° (bodies d and e in Fig. 8.14B) and recovered magnetisation direction even more closely with errors of only 4° and 1° (possibly because minimum and maximum extension are not coincident with the axes of grid reflection). These results confirm that MCS analysis is suitable for bodies with horizontal elongation at least up to a factor of 2.

8.5 CONCLUSIONS

We have shown that the 3 × 3 matrix of magnetic field–magnetisation components for a dipole with positive unit magnetisation along each principal axis is identical

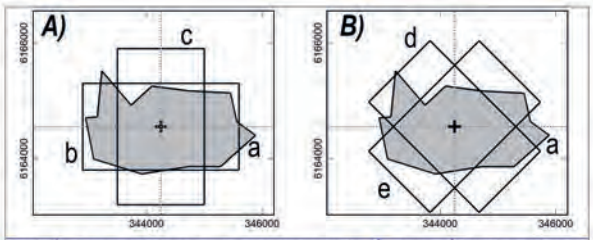

model	Recovered Magnetization direction estimate	error	Individual estimates
a	226.2°, +10.1°	5.8°	234, 220, 225 +10, +10, +11
b	225.1°, +9.3	6.8°	232, 219, 224 +9, +9, +10
c	238.6°, +7.1°	6.8°	232, 244, 240 +4, +9, +9
d	228.5°, +7.2°	3.9°	227, 230, 229 +7, +7, +8
e	231.7°, +9.9°	1.0°	230, 233, 232 +9, +10, +11

Fig. 8.14. Magnetisation directions recovered by MCS analysis of fields computed from the bodies shown in A) and B) with input magnetisation direction of 232°, +8°.

to the gravity gradient tensor of a point mass. For bodies with a vertical axis of fourfold symmetry the direction of magnetisation can be estimated by analysis of field components with specified symmetry characteristics ascribed to specific magnetisation components. The fields of contributions from each orthogonal magnetisation component are isolated by a series of operations on field component grids (transformed from the TMI grid) reflected about north–south and east–west planes through the horizontal centre of magnetisation. The analysis has been successfully applied to computed magnetic fields of complex symmetric bodies and provides an acceptable magnetisation estimate for the measured BHN-NW aeromagnetic anomaly. Analysis of model-computed fields shows that the analysis is reasonably tolerant of departure from ideal symmetry. Further studies are required to establish sensitivity to estimation of the centre of magnetisation but MCS analysis appears well suited for first-pass rapid automated studies.

REFERENCES

Beiki M, Clark DA, Austin JR, Foss CA (2012) Estimating source location using normalized magnetic source strength calculated from magnetic gradient tensor data. *Geophysics* **77**, J23–J37. doi:10.1190/geo2011-0437.1

Blakely RJ (1995) 'Potential theory in gravity and magnetic applications'. (Cambridge University Press).

Caratori Tontini F, Pedersen LB (2008) Interpreting magnetic data by integral moments. *Geophysical Journal International* **174**, 815–824. doi:10.1111/j.1365-246X.2008.03872.x

Clark DA (2014) Methods for determining remanent and total magnetisations of magnetic sources – a review. *Exploration Geophysics* **45**, 271–304. doi:10.1071/EG14013

Dannemiller N, Li Y (2006) A new method for determination of magnetisation direction. *Geophysics* **71**, L69–L73. doi:10.1190/1.2356116

Dransfield MH (1994) Airborne gravity gradiometry. Doctor of Philosophy, The University of Western Australia. doi:10.26182/5c89d3c7789f1

Fedi M, Florio G, Rapolla A (1994) A method to estimate the total magnetisation direction from a distortion analysis of magnetic anomalies. *Geophysical Prospecting* **42**, 261–274. doi:10.1111/j.1365-2478.1994.tb00209.x

Foss CA (2006) 'Evaluation of strategies to manage remanent magnetisation effects in magnetic field inversion.' 76th Annual International Meeting, SEG, Expanded Abstracts, 938–942.

Foss CA (2017) 'Resultant-magnetisation based magnetic field interpretation' in V. Tschirhart and M.D. Thomas eds, Proceedings of Exploration 17: Sixth Decennial International Conference on Mineral Exploration, pp. 637–648.

Foss CA, McKenzie KB (2011) Inversion of anomalies due to remnant magnetisation: an example from the Black Hill Norite of South Australia. *Australian Journal of Earth Sciences* **58**, 391–405. doi:10.1080/08120099.2011.581310

Fullagar PK, Pears GA (2015) 'Remanent magnetisation inversion.' 24th ASEG International Geophysical Conference, Extended Abstracts. doi:10.1071/ASEG2015ab188

Helbig K (1963) Some integrals of magnetic anomalies and their relation to the parameters of the disturbing body. *Zeitschrift für Geophysik* **29**, 83–96.

Lelièvre PG, Oldenburg DW (2009) A 3D total magnetisation inversion applicable when significant, complicated remanence is present. *Geophysics* **74**, L21–L30. doi:10.1190/1.3103249

Li Y (2012) Recent advances in 3D generalized inversion of potential-field data. *SEG Technical Program Expanded Abstracts* **2012**, 1–7.

Lourenço JS, Morrison HF (1973) Vector magnetic anomalies derived from measurements of a single component of the field. *Geophysics* **38**, 359–368. doi:10.1190/1.1440346

McKenzie KB, Foss CA, Hillan D (2012) 'An improved search for magnetisation direction.' 22nd ASEG Geophysical Conference, Extended Abstracts, 1–4.

Paine J, Haederle M, Flis M (2001) Using transformed TMI data to invert for remanently magnetised bodies. *Exploration Geophysics* **32**, 238–242. doi:10.1071/EG01238

Pedersen LB, Bastani M (2016) Estimating rock vector magnetisation from coincident measurements of magnetic field and gravity gradient tensor. *Geophysics* **81**, B55–B64. doi:10.1190/geo2015-0100.1

Pedersen LB, Rasmussen TM (1990) The gradient tensor of potential field anomalies: some implications on data collection and data processing of maps. *Geophysics* **55**, 1558–1566. doi:10.1190/1.1442807

Phillips JD (2005) Can we estimate total magnetisation directions from aeromagnetic data using Helbig's integrals? *Earth, Planets, and Space* **57**, 681–689. doi:10.1186/BF03351848

Phillips JD, Nabighian MN, Smith DV, Li Y (2007) Estimating locations and total magnetisation vectors of compact magnetic sources through combined Helbig and Euler analysis. *SEG Technical Program Expanded Abstracts* **26**, 770–774.

Pratt DA, McKenzie KB, White AS (2014) Remote remanence determination (RRE). *Exploration Geophysics* **45**, 314–323. doi:10.1071/EG14031

Rajagopalan S, Schmidt PW, Clark DA (1993) Rock magnetism and geophysical interpretation of the Black Hill Norite, South Australia. *Exploration Geophysics* **24**, 209–212. doi:10.1071/EG993209

Schmidt PW, Clark DA (1997) Directions of magnetisation and vector anomalies derived from total field surveys. *Preview* **70**, 30–32.

Schmidt PW, Clark DA (1998) The calculation of magnetic components and moments from TMI: a case study from the Tuckers igneous complex, Queensland. *Exploration Geophysics* **29**, 609–614. doi:10.1071/EG998609

Schmidt PW, Clark DA, Rajagopalan S (1993) An historical perspective of the Early Palaeozoic APWP of Gondwana: new results from the Early Ordovician Black Hill Norite of South Australia. *Exploration Geophysics* **24**, 257–262. doi:10.1071/EG993257

Turner SP (1991) Late-orogenic, mantle-derived, bimodal magmatism in the southern Adelaide Foldbelt, South Australia. PhD thesis, University of Adelaide (unpubl.).